Results in Physics 13 (2019) 102344

Contents lists available at ScienceDirect

Results in Physics

journal homepage: www.elsevier.com/locate/rinp

Ultrasound induced green synthesis of pyrazolo-pyridines as novel corrosion inhibitors useful for industrial pickling process: Experimental and theoretical approach

Parul Dohare[a], M.A. Quraishi[b,*], Chandrabhan Verma[c,d,*], H. Lgaz[e], R. Salghi[f], E.E. Ebenso[c,d,*]

[a] Department of Chemistry, Indian Institute of Technology, Banaras Hindu University, Varanasi 221 005, India
[b] Center of Research Excellence in Corrosion, Research Institute, King Fahd University of Petroleum and Minerals, Dhahran 31261, Saudi Arabia
[c] Department of Chemistry, School of Chemical and Physical Sciences, Faculty of Natural and Agricultural Sciences, North-West University, Private Bag X2046, Mmabatho 2735, South Africa
[d] Material Science Innovation & Modelling (MaSIM) Research Focus Area, Faculty of Natural and Agricultural Sciences, North-West University, Private Bag X2046, Mmabatho 2735, South Africa
[e] Laboratory of Separation Methods, Faculty of Science, IbnTofail University PO Box 242, Kenitra, Morocco
[f] Laboratory of Applied Chemistry and Environment, ENSA, IbnZohr University, PO Box 1136, 80000 Agadir, Morocco

ARTICLE INFO

Keywords:
Inhibition
Pyrazolopyridine
Adsorption
DFT
MD Simulation
Diffusion model

ABSTRACT

Three pyrazolo-pyridine derivatives namely, (PPs) (4-(4-methoyphenyl)3,5-dimethyl-1,4,7,8-tetrahydrodipyrazolopyridine) (PP-1), 3,5dimethyl-4-phenyl-1,4,7,8-tetrahydrodipyrazolopyridine (PP-2) and (3,5-dimethyl-4-(3-nitrophenyl)-1,4,7,8-tetrahyddrodipyrazolopyridine) (PP-3) having different substituents was synthesized using ultrasound mediated one step multicomponent reactions and evaluated as corrosion inhibitors for mild steel in acidic medium of 1 M HCl. Protection ability of the synthesized PPs was determined using several experimental and computational modeling methods. Results showed that PP-3 having electron withdrawing nitro ($–NO_2$) substituent showed lowest inhibition ability and PP-1 having electron releasing methoxy ($–OCH_3$) substituent showed the highest inhibition efficiency. Inhibition efficiencies of the tested PP molecules followed the order: PP-1 (96.4%; $–OCH_3$) > PP-2 (94.2%; –H) > PP-1 (91.1%; $–NO_2$). Electrochemical studies suggested that PPs acted as interface and mixed type of corrosion inhibitors and their adsorption at the metal-electrolyte interfaces obeyed the Langmuir adsorption isotherm model. SEM and AFM analyses were adopted to measure the surface morphology of inhibited and uninhibited metallic surfaces. Experimental results were corroborated by results derived from DFT modeling and MD simulations.

Introduction

Ultrasound-assisted synthesis has recently emerged as a powerful and green approach for synthesis of organic compounds which can be used as corrosion inhibitors. It offers several benefits compared with conventional techniques. In some cases, ultrasonic irradiation can increase reactivity by several fold [1,2]. It takes place through the process of acoustic cavitation i.e. the formation, growth, and implosive collapse of bubbles in liquid. A large number of organic reactions can be carried out under ultrasonic irradiation with a short reaction time, high yield, and milder conditions [3–6]. While, Conventional thermal methods used for synthesizing organic inhibitors are expensive, take long reaction times involving harsh reaction conditions. Pyrazolopyridine is a promising class of heterocyclic compounds. They exhibit a wide range of biological activities, such as antimicrobial, insecticidal, and anti-inflammatory properties, and they are also used for the treatment of several diseases, including bipolar disorder, diabetes, dementia, Alzheimer's disease, schizophrenia, depression, and cancer [7–10].

A literature survey revealed that a number of methods have been reported for the synthesis of pyrazolopyridines [11–13] but all these methods suffered from drawbacks such as longer reaction time, lower yield, use of hazardous organic solvents and reagents, tedious workup procedures, and co-occurrence of several side reactions with less selectivity of the process. A few of the pyrazolopyridine compounds have been investigated as corrosion inhibitors for metals and alloys in acid medium such as, Sorkhabi et al. [14] investigated Schiff base derived

* Corresponding authors at: Department of Chemistry, School of Chemical and Physical Sciences, Faculty of Natural and Agricultural Sciences, North-West University, Private Bag X2046, Mmabatho 2735, South Africa (C. Verma and E.E. Ebenso).
E-mail addresses: maquraishi.apc@itbhu.ac.in (M.A. Quraishi), chandraverma.rs.apc@itbhu.ac.in (C. Verma), Eno.Ebenso@nwu.ac.za (E.E. Ebenso).

https://doi.org/10.1016/j.rinp.2019.102344
Received 16 March 2019; Received in revised form 9 May 2019; Accepted 9 May 2019
Available online 17 May 2019

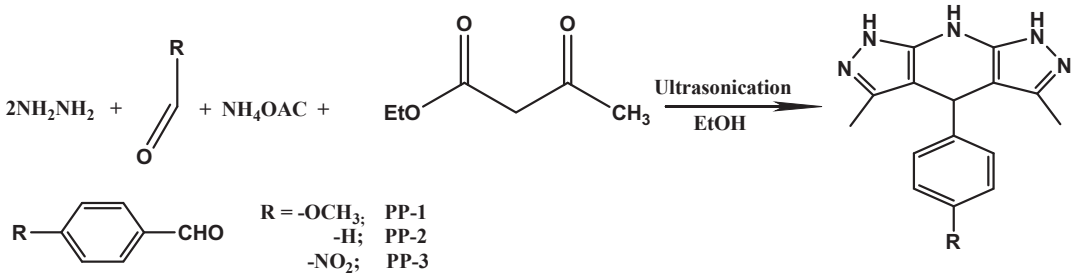

Fig. 1. Synthetic scheme for the synthesis of PP molecules.

Table 1
Molecular structure and analytical data of PPs.

Inhibitor	Structure	Analytical data
4-(4-Methoyphenyl) 3,5-dimethyl-1,4,7,8-tetrahydrodipyrazolo pyridine) (PP-1)	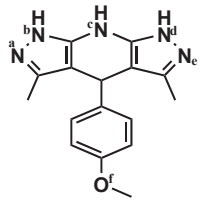	White crystalline powder; m.p = 321–323 °C; ^{1}H NMR (500 MHz, DMSO) δ (ppm): 1.48, 3.77, 4.38, 4.63, 6.87–7.32, 10.93, 11.96
3,5dimethyl-4-phenyl-1,4,7,8-tetrahydrodipyrazolopyridine (PP-2)	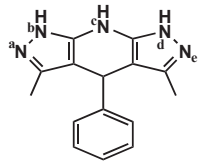	White crystalline powder; m.p = 271–273 °C; 1H NMR (500 MHz, DMSO) δ (ppm): 1.49, 4.65, 4.41, 7.12–7.56, 6.87–7.32, 10.96, 11.99
3,5-dimethyl-4-(3-nitrophenyl)-1,4,7,8-tetrahyddrodipyrazolo pyridine) (PP-3)	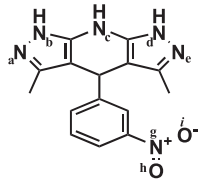	Pale yellow crystalline powder ; m.p = 271–273 °C; 1H NMR (500 MHz, DMSO) δ (pp): 1.93, 4.0, 5.34, 7.53–8.16, 7.59 12.62

from2 amino pyridine as corrosion inhibitors. These compounds exhibited maximum IE of 85–95% at 200 mg L^{-1}. Yan Ji et al. [15] reported corrosion inhibition action of pyridin-2-ylmethyl-N,N-diethylaniline (BPMA) shows corrosion inhibition efficiency 88.1% at 450 ppm. Mhammedi et al. [16] studied the corrosion inhibition behavior of pyrazole fused with pyridine as corrosion inhibitors on mild steel in IM HCl solution. These authors have reported 92% IE at 150 mg L^{-1}. Singh et al. [17] investigated corrosion inhibition effect of tetrahydro-2H-pyrazolo [3,4-b] pyridine derivatives on mild in 1 M HCl. These compounds exhibited maximum IE 85–95% at 200 mg L^{-1}. In our earlier publication [18] we have synthesized fused pyrano-pyrazole derivatives. These compounds showed inhibition efficiency of 97–98% at concentration as low as 100 mg L^{-1}. In view of the better performance of condensed heterocyclic compounds as corrosion inhibitors than single ring compounds, In the present work, we wish to report the synthesis of pyrazolopyridine derivatives under ultrasound irradiation, namely, (4-(4-methoyphenyl)3,5-dimethyl-1,4,7,8-tetrahydrodipyrazolopyridine) (PP-1), 3,5dimethyl-4-phenyl-1,4,7,8-tetrahydrodipyrazolopyridine (PP-2) and (3,5-dimethyl-4-(3-nitrophenyl)-1,4,7,8-tetrahyddrodipyrazolopyridine) (PP-3) and studied their corrosion inhibition performance on mild steel in 1 M HCl using gravimetric, potentiodynamic polarization measurements, electrochemical impedance spectroscopy. Surface morphology of the inhibited MS specimens was examined by scanning electron microscope (SEM), atomic force microscopy (AFM).

Density functional theory (DFT) and Molecular dynamics have been used to predict the reactivity and adsorption behavior of inhibitors molecules on the metal surface. A good correlation has been found between these methods. Pyrazolo-pyridine inhibitors showed better performance (97% IE at 100 mg L^{-1}) than hexamine (90% IE at 100 mg L^{-1}). Hexamine is used in industry as pickling inhibitor Also the use of hexamine is not safe due to its toxicity which limits its practical application. The survey of literature reveals that these pyrazolo-pyridine derivatives (PPs) have not been investigated as corrosion inhibitors.

Experimental

Materials and solution

MS specimens, having composition (in wt %) 0.076C, 0.012P, 0.026Si, 0.192 Mn, 0.050 Cr, 0.135 Cu, 0.023 Al, 0.050 Ni and the remainder iron, The MS was successively cleaned with emery papers of different grade (600, 800, 1000, and 1200), washed with de-ionized water, degreased with acetone, ultrasonically cleaned with ethanol and dried, before being used in the experiments. Hydrochloric acid (HCl, 37%) and double distilled water were used for preparation of test solution (1 M HCl).

Synthesis of inhibitors

A mixture of hydrazine hydrate (2.0 mmol), β-dicarbonyl compound (2.1 mmol), appropriate substituted aldehydes (1.0 mmol) and (4.0 mmol) of ammonium acetate in 10 mL EtOH was introduced in a heavy walled beaker. The beaker was attached to a 12 mm tip diameter probe, and the

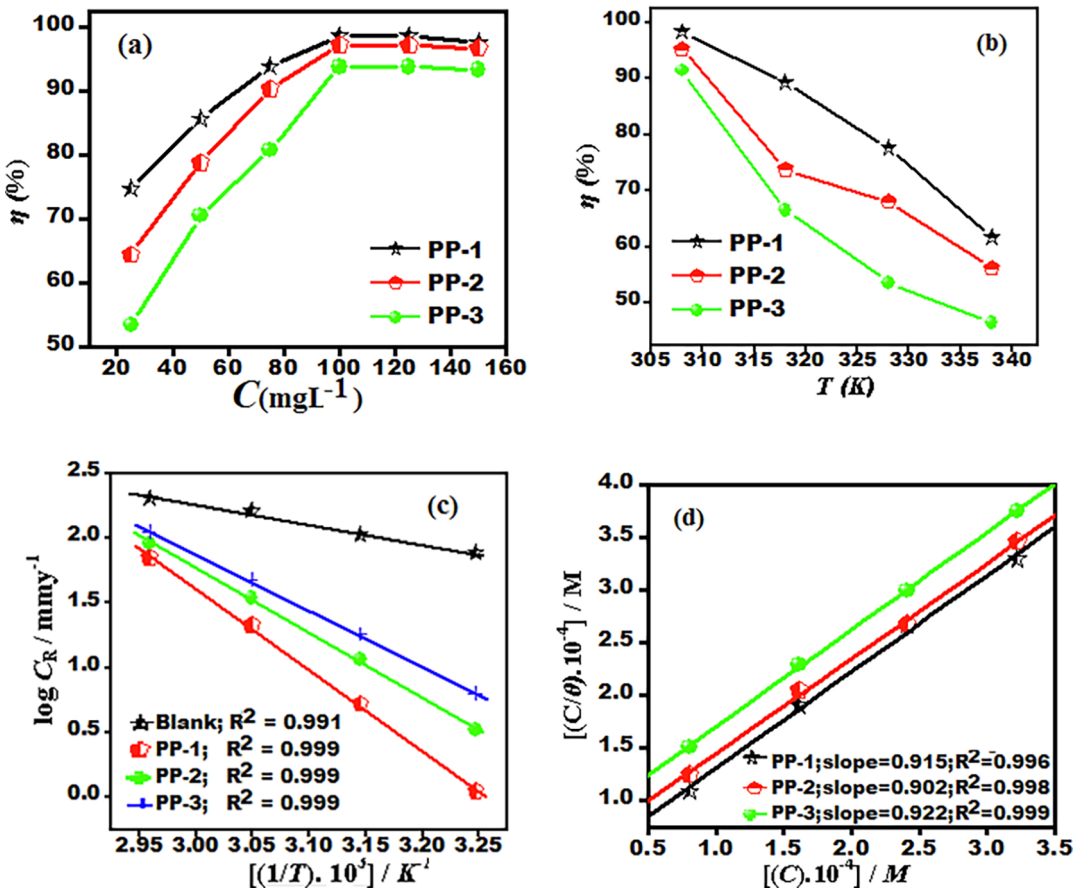

Fig. 2. (a): Variation of inhibition efficiency (η%) with inhibitor concentration at 308 K. (b): Variation of inhibition efficiency (η%) with solution temperature (308–338 K) at optimum concentration of PPs. (c): Arrhenius plots of the corrosion rate (CR) of mild steel in absence and presence of optimum concentration of PPs. (d): Langmuir adsorption isotherm plots.

Table 2
Thermodynamic and activation parameters for mild steel corrosion in 1 M HCl at optimum concentration (100 mg L^{-1}) of PP molecules.

Inhibitor	K_{ads} (10^4 M^{-})	$-\Delta G^{\circ}_{ads}$ (kJ mol^{-1})	E_a (kJ mol^{-1})
Blank	–	–	28.74
PP-1	2.5	36.26	120.04
PP-2	1.8	35.38	95.54
PP-3	1.2	34.51	83.06

Table 3
Slope and correlation coefficient values for different tested adsorption isotherm for the adsorption of PP molecules on metallic surface at 308 K.

Adsorption isotherm	Inhibitor	Correlation coefficient	Slope
Langmuir	PP-1	0.996	0.997
	PP-2	0.998	0.987
	PP-3	0.999	0.945
Temkin	PP-1	0.884	0.048
	PP-2	0.897	0.037
	PP-3	0.897	0.014
Frumkin	PP-1	0.885	4.367
	PP-2	0.886	4.369
	PP-3	0.875	0.602

reaction mixture was sonicated for the specified period at 50% power of the processor and in a 5 s pulse mode until a solid product separates out. Completion of the reaction was monitored by TLC using n-hexane:ethyl acetate (7:3) as the eluent. All the reactions were invariably complete in 30–40 min. The scheme is shown in Fig. 1 (Scheme 1). The molecular structure, analytical data and abbreviations of the inhibitors are given Table 1.Ultrasound irradiation was provided by an ultrasonic processor probe (Processor Sonics and material inc. VCX75 S/N 79348AE-03-14Ultrasonics with power input 230 V, 50 Hz, 8 Amps, and power variac 0–230 V and 8 Amps) operating at 20 kHz and 750 W with 6 mm/12 mm tip diameter probes. Earlier these compounds were synthesized by chemical method under reflux condition in 4–8 hr [19].

Gravimetric experiment

Gravimetric experiment was performed according to ASTM standard method [20]. The corrosion rates CR (mg cm^2 h^{-1}) were calculated using equations.

$$C_R = \frac{w}{dAt} \quad (1)$$

Here, w is the weight loss of MS coupon, A is the total area of a MS coupon; t is immersion time (3 h) d is the density in g cm^{-3}. With the calculated corrosion rate, the inhibition efficiency η% was calculated as follows [21]

$$\eta\% = \frac{C_R - C_{R(i)}}{C_R} \times 100 \quad (2)$$

The surface coverage (θ) was calculated using following equations:

$$\theta = \frac{C_R - C_{R(i)}}{C_R} \quad (3)$$

where C_R is the corrosion rate in absence and $C_{R(i)}$ presence of inhibitors.

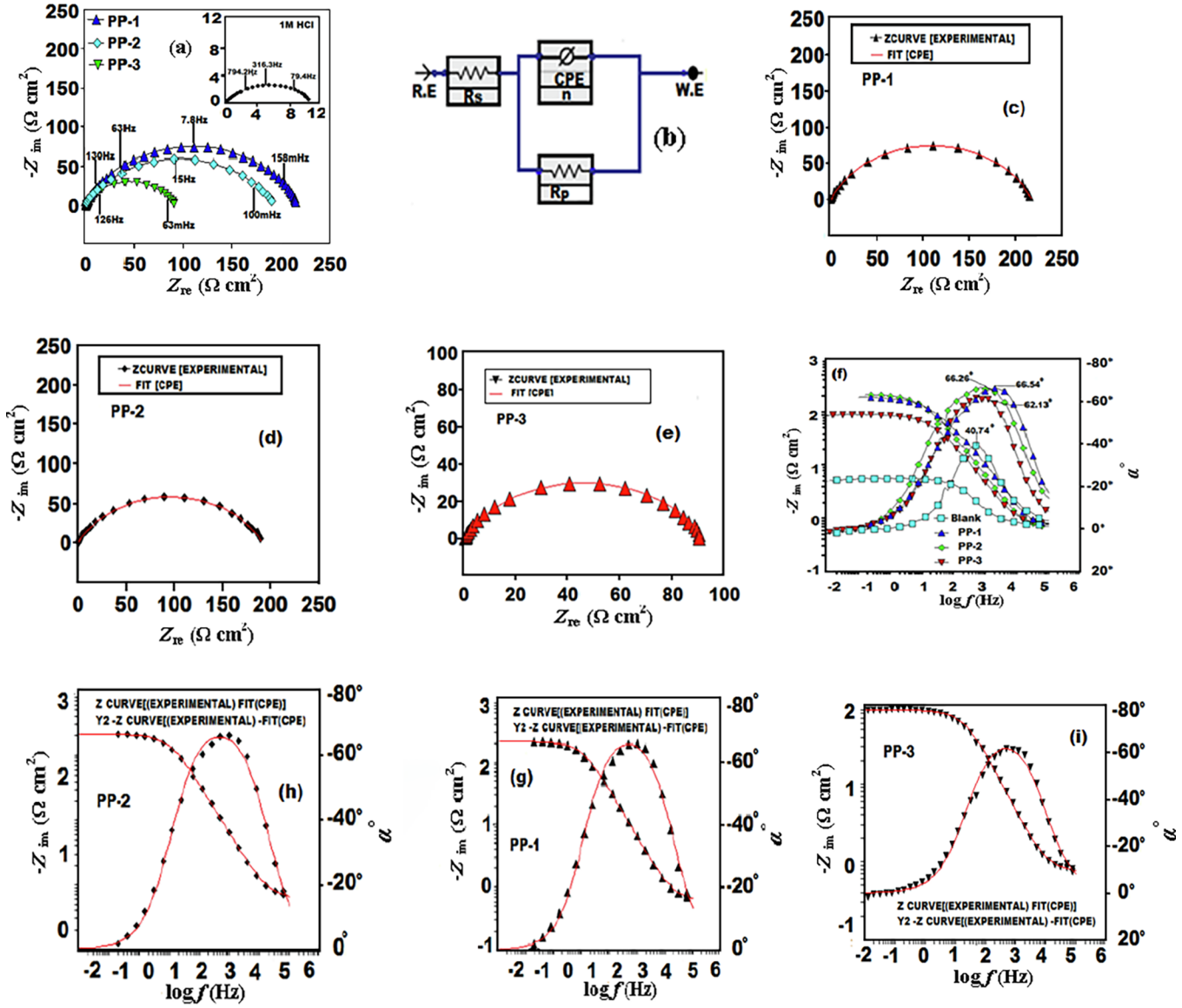

Fig. 3. (a): Nyquist plots for the mild steel at optimum concentration of PPs. (b): Equivalent circuit model used to fit the EIS data. (c-e) Fitted Nyquist (c) PP-1 (d) PP-2 (e) PP-3. (f-h): Fitted Bode plot (f) PP-1 (g) PP-2 (h) PP-3. (i): Bode (log f vs. log |Z|) and phase angle (log f vs. α∘) plots in the absence and presence of optimum concentration of PPs at 308 K.

Table 4
Electrochemical impedance parameters (± SD) for mild steel in 1 M HCl in the absence and presence of optimum concentration (100 mg L^{-1}) of PPs at 308 K.

Inhibitor	R_s (Ω)	R_p (Ω cm^2)	N	Y_0 (μF/cm^2)	C_{dl} (μF/cm^2)	η (%)
Blank	1.02(0.02)	7.44 (0.02)	0.798	481.2	137.9	–
PP-1	0.615(0.02)	221.4(0.02)	0.853	85.9	48.0	96.63
PP-2	0.653(0.02)	116.52(0.02)	0.818	170.2	76.8	93.61
PP-3	0.758(0.02)	86.4(0.02)	0.807	250.5	103.2	91.38

Electrochemical method

The MS specimens with exposed area of 1 cm^2 were utilized for all electrochemical measurements under potentiodynamic condition by using Gamry Potentiostat/Galvanostat (Model G-300) instrument. Gamry Echem Analyst 5.5 software was used to fit and analyzed all electrochemical data. The instrument consists of a MS as working electrode (WE), platinum as a counter electrode and a saturated calomel electrode (SCE) as a reference electrode. Before starting the electrochemical experiments, the working electrode was allowed to corrode freely for 30 min in order to attain steady open circuit potential (OCP). During polarization measurements, the cathodic and anodic Tafel slopes were recorded by changing the electrode potential from −0.250 to +0.250 V vs. corrosion potential (E_{corr}) at a constant sweep rate of 1.0 mV s^{-1}. The corrosion current density (i_{corr}) was calculated by extrapolating the linear segments of Tafel slopes and the inhibition efficiency was calculated using the following relation [20]:

$$\eta\% = \left(1 - \frac{i_{corr(inh)}}{i_{corr}}\right) \times 100 \quad (4)$$

where, $i_{corr(i)}$ and i_{corr} are corrosion currents, in the presence and absence of PPs, respectively. Electrochemical impedance measurements were carried out at open circuit potential in the frequency range of 100 kHz to 0.01 Hz using AC signal of amplitude 10 mV peak to peak. The polarization resistances were calculated from Nyquist plots. The inhibition efficiency was calculated using following equation [22]:

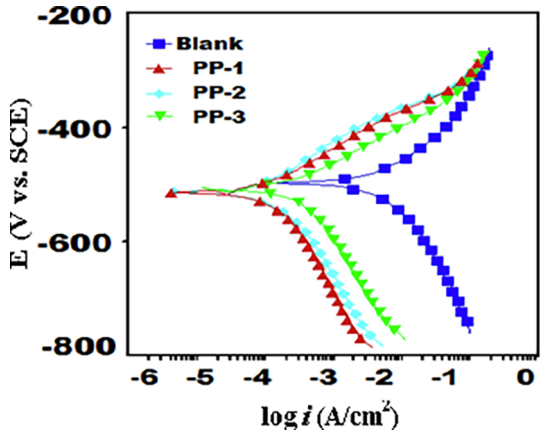

Fig. 4. Polarization curves for corrosion of mild steel in the absence and presence of optimum concentrations of PP molecules.

Table 5
Potentiodynamic polarization parameters (± SD) for mild steel in 1 M HCl in the absence and presence of optimum concentration (100 mg L^{-1}) of PPs at 308 K.

Inhibitor	E_{corr} (mV/SCE)	i_{corr} (μA/cm^2)	β_a (mV/dec)	$-\beta_c$ (mV/dec)	η (%)
Blank	−445	1320(0.03)	74.6	123.9	–
PP-1	−513	49.9 (0.04)	84.3	174.3	96.21
PP-2	−512	68.0(0.04)	83.9	170.3	94.84
PP-3	−506	74.7 (0.03)	69.5	153.6	94.34

$$\eta\% = \left(\frac{R_{p(i)} - R_p}{R_{p(i)}}\right) \times 100 \quad (5)$$

where, R_p (sum of R_{ct} and R_f) and $R_{p(i)}$ respectively represent the polarization resistance in absence and presence of optimum concentration of inhibitors.

Surface study (SEM and AFM)

The MS coupons were exposed in 1 M HCl solution, in the absence and presence of optimum concentration (100 mg L^{-1}) of PPs for 3 h at room temperature. SEM study was carried out at an accelerating voltage of 5 kV and 5 k × magnification by using a Ziess EVO 50 XVP instrument, and AFM study was done using NT-MDT multimode, Russia, controlled by a solver scanning probe microscope controller.

Quantum chemical calculations

Quantum chemical calculations were performed using density functional theory (DFT) with the Beck's three parameter exchange functional along with the Lee-Yang–Parr nonlocal correlation functional (B3LYP) with 6-31G (d, p) basis set using Gaussian 03 program [23,24]. All the theoretical parameters obtained were E_{HOMO}, E_{LUMO}, ΔE (E_{LUMO}-E_{HOMO}),Mullikan charge on heteroatoms (N, O), and dipole moment (μ). Other parameters such as hardness (η), softness (σ), global electro negativity (χ), and the fraction of electron transfer (ΔN), from the metal atom were calculated according to the following equations respectively [25,26].

$$\Delta E = E_{LUMO} - E_{HOMO} \quad (6)$$

$$\eta = \frac{1}{2}(E_{LUMO} - E_{HOMO}) \quad (7)$$

$$\sigma = \frac{1}{\eta} \quad (8)$$

$$\chi = -\frac{1}{2}(E_{LUMO} + E_{HOMO}) \quad (9)$$

$$\Delta N = \frac{\phi - \chi_{inh}}{2(\eta_{Fe} + \eta_{inh})} \quad (10)$$

where ϕ and η_{inh} denote the is work function and electronegativity of iron and inhibitor, respectively. A value of 4.82 was used for the ϕ, while η_{Fe} was taken as 0 for bulk Fe atom [15].

The Fukui functions were calculated using the UCA-FUKUI v 1.0 software [27] via Finite Difference (FD) method with the use of the output file from Gaussian 03. The Fukui function (f_k) is the first derivative of the electronic density $\rho(\vec{r})$ with respect to the number of electrons N, in a constant external potential $\upsilon(\vec{r})$ and written as follows:

$$f_k = \left(\frac{\partial\rho(\vec{r})}{\partial N}\right)_{\upsilon(\vec{r})} \quad (11)$$

Finite difference approximations have been used to get Fukui functions in favor of nucleophilic and electrophilic attacks as [28–30]:

$$f_k^+ = q_k(N+1) - q_k(N) \text{(For nucleophilic attack)} \quad (12)$$

$$f_k^- = q_k(N) - q_k(N-1) \text{(For electrophilic attack)} \quad (13)$$

$$f_k^0 = \frac{q_k(N+1) - q_k(N-1)}{2} \quad (14)$$

Here, gross charge of the atom k is denoted by q_k. The q_k $(N+1)$, q_k (N) and q_k $(N-1)$ are the charges of the anionic, neutral and cationic species, respectively.

Molecular dynamic simulations

Molecular modeling details

MD simulations were carried out in a simulation box with periodic boundary conditions using Materials Studio 6.0 (from Accelrys Inc.) [31]. The iron crystal was imported and cleaved along (1 1 0) plane and a slab of 5 Å was employed. The Fe (1 1 0) surface was relaxed by minimizing its energy using smart minimiser method. Fe (1 1 0) surface was enlarged to a (10 × 10) super cell to provide a large surface for the interaction of the inhibitors. A vacuum slab with zero thickness was built. A supercell with a size of a = b = 24.82 Å c = 25.14 Å, contains 500 H_2O, $5H_3O^+$, $5Cl^-$ and one molecule of tested inhibitors was created. The simulation was carried out in a simulation box (24.82 × 24.82 × 35.69 $Å^3$) using discover module with a time step of 1 fs and simulation time of 500 ps performed at 303 K, NVT ensemble (constant number of atoms, constant-volume, constant-temperature)

Table 6
Mullikan charge on different heteroatoms of PP molecules.

Inhibitors	Mullikan charge on heteroatom's								
	N_a	N_b	N_c	N_d	N_e	N_g	O_f	O_h	O_i
PP-1	−0.404	−0.410	−0.760	−0.419	−0.411	–	−0.516	–	–
PP-2	−0.404	−0.409	−0.760	−0.418	−0.411	–	–	–	–
PP-3	−0.402	−0.402	−0.761	−0.412	−0.409	−0.241	–	−0.415	−0.419

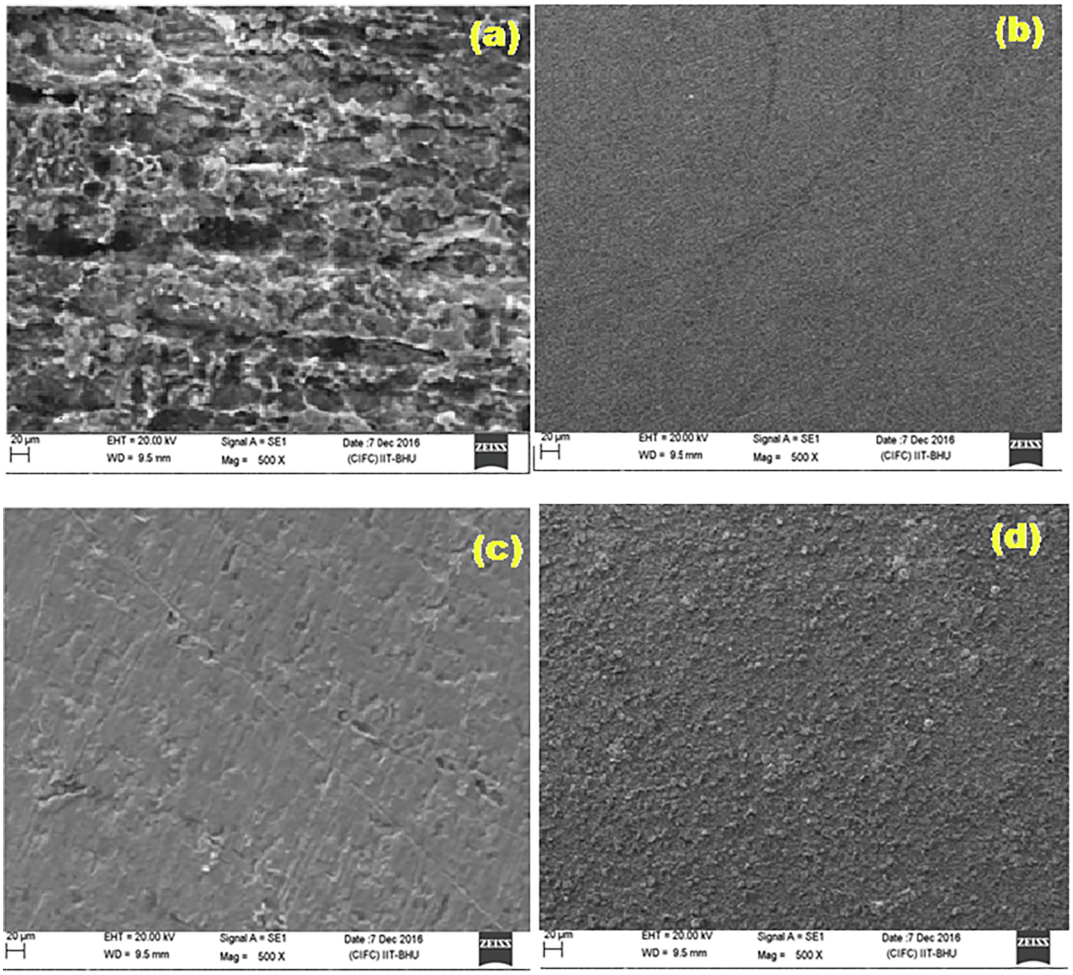

Fig. 5. SEM images of corroded metallic surface in the absence (a) and presence of (b) PP-1 (c) PP-2 (d) PP-3 molecule.

and COMPASS force field [28]. In simulation system, the interactions between the inhibitor and Fe (1 1 0) can be understood by interaction and binding energies calculated using Eqs. (1) and (2) [32,33]:

$$E_{\text{interaction}} = \text{E}_{\text{total}} - (\text{E}_{\text{surface + solution}} + \text{E}_{\text{inhibitor}}) \quad (15)$$

$$E_{\text{Binding}} = -\text{E}_{\text{interaction}} \quad (16)$$

where E_{total} is the total energy of the entire system $E_{\text{surface + solution}}$ referred to the total energy of Fe (1 1 0) surface and solution without the inhibitor and $E_{\text{inhibitor}}$ represent the total energy of inhibitor.

Results and discussion

Gravimetric measurement

Inhibitor concentration effect

Fig. 2(a) shows variation in efficiency with inhibitors concentration. From Fig. 2(a) it is revealed that on increasing the inhibitor concentration, the inhibition efficiency increased. The maximum inhibition efficiency was obtained for PP-1 sowed maximum IE 97.5% among the three studied inhibitors at optimum concentration 100 mg L^{-1}. The inhibition efficiency of PPs follows the order: PP-1 > PP-2 > PP-3 respectively at 100 mg L^{-1}. The maximum inhibition efficiency for PP-1 was 97.5% at 100 mg L^{-1} the better performance of PP-1 was due to the presence of electron donating methoxy group, and lower I.E of PP-3 is attributed to the presence of electron withdrawing NO_2 group.

Temperature effect

The effect of temperature on the inhibition efficiency (η%) of PPs was studied on MS in the temperature range of 308–338 K in 1 M HCl for 3 h immersion time at optimum concentration (100 mg L^{-1}) of PPs. From the Fig. 2(b), it is clear that inhibition efficiency (η%) slightly decreased with increase in temperature, which is attributed to partial desorption of the PPs molecules from the MS surface [13]. The Arrhenius plot, which is the linear function of logarithm of C_R vs. $1/T$ and given by the following equation:

$$\log(C_R) = \frac{-E_3}{2.303RT} + \log A \quad (17)$$

where, E_a represents the apparent activation energy and λ denotes the pre-exponential factor. The activation energy was calculated by plotting a graph between log C_R and $1/T$ and is represented in Fig. 2(c). From the slope of the obtained straight line, the activation energy was calculated and presented in Table 2. An inspection of Table 2 reveals that the values of activation energy are more in presence of inhibitors than in their absence [35,36]. This indicates that as the temperature increased there is an appreciable decrease in the adsorption of inhibitors, which in turn increases the corrosion rate because more metal steel surface area is now exposed to the acidic environment [37–39].

Adsorption consideration

The adsorption behavior of inhibitor molecules on mild steel surface can be studied by using adsorption isotherms. The commonly used adsorption isotherms in corrosion study are Frumkin, Langmuir and Temkin, in this study, Langmuir adsorption isotherm, which is a plot of

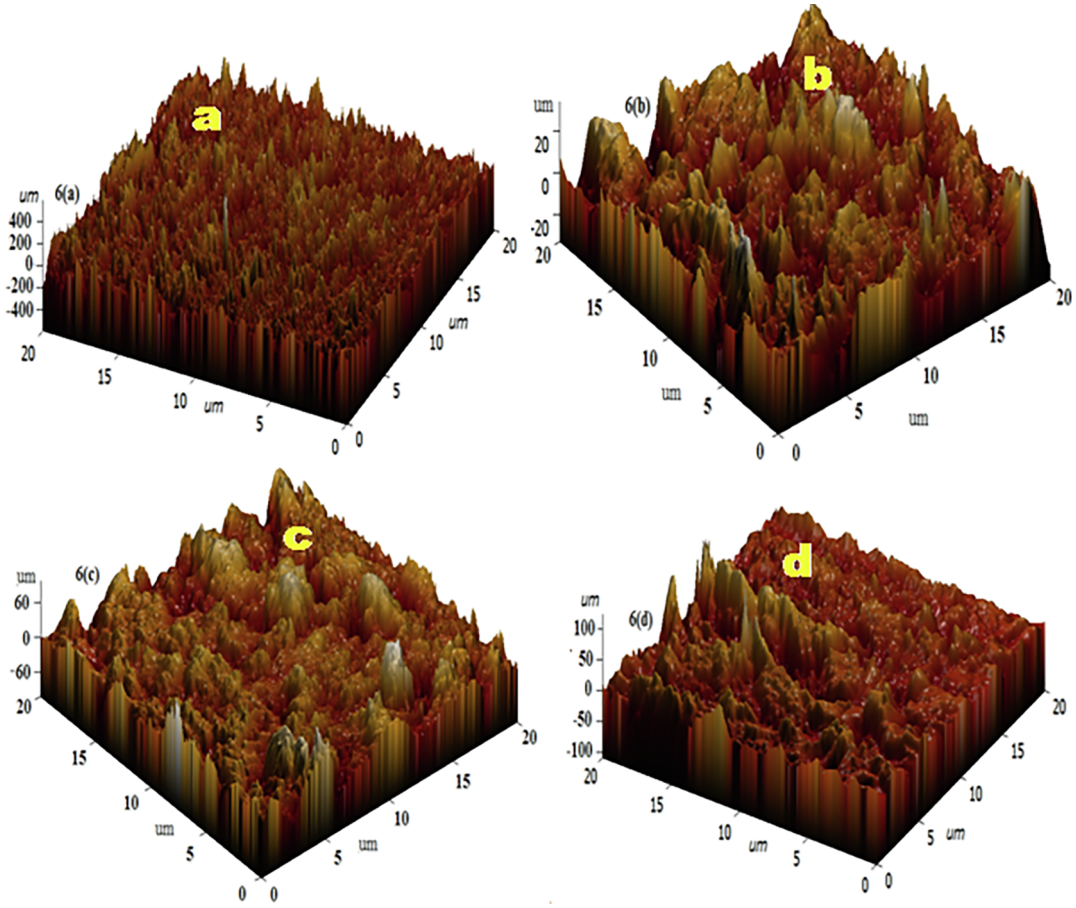

Fig. 6. AFM images of corroded metallic surface in the absence (a) and presence of (b) PP-1 (c) PP-2 (d) PP-3 molecule.

C/θ vs C was found to be the best fit because their R^2 and slope values are close to 1 and are shown in Fig. 2d and the result listed in Table 3. The Langmuir adsorption isotherm can be given by the following equation [40].

$$C/\theta = 1/K_{ads} + C \tag{18}$$

where θ is the surface coverage, C is the inhibitor concentration, K_{ads} is the equilibrium constant of adsorption process. K_{ads} is calculated from the intercepts of the straight lines, and it is correlated with the standard free energy of adsorption (ΔG_{ads}) by the following equation [37].

$$\Delta G^{o}_{ads} = -RT\ln(55.5K_{ads}) \tag{19}$$

where R is the gas constant and T is the absolute temperature. The value of 55.5 is the concentration of water in solution in mol L^{-1}. The equilibrium constant value of adsorption (K_{ads}) and standard free energy of adsorption (ΔG°_{ads}) are listed in Table 2. The calculated values of ΔG°_{ads} for studied inhibitors range from -36.26 to -34.51 kJmol^{-1} which indicate their mixed mode of adsorption on to the MS surface [41,42]. Also higher values of K_{ads} suggest a higher inhibition effect.

Electrochemical measurements

Electrochemical impedance spectroscopy

The electrochemical impedance measurements in the absence and presence of PPs at their optimum concentration (100 mg L^{-1}) are shown in Fig. 3(a),it is observed from Fig. 3(a), that the diameter of semicircle significantly increases on the addition of the PPs [43]. The Nyquist plots show single capacitive semi-circles loop which indicates that corrosion inhibition is governed by the charge-transfer process. Also these semi circles loops are depressed with their centers under the real axis, which is due to the surface roughness and frequency dispersion [44,45]. All the impedance parameters were calculated from the equivalent circuit model shown in Fig. 3(b), which consists of (Rs) is the solution resistance, (R_p) is the polarization resistance and *CPE* is the constant phase element. The fitness accuracy of the used equivalent circuit is shown by the fitted Nyquist plots of PPs [Fig. 3(c-e)]. The impedance, Z_{CPE} of constant phase element, is expressed as [46]

$$Z_{CPE} = Y_0^{-1}(j\omega)^{-n} \tag{20}$$

where Yo is the magnitude, j is the square root of -1, ω is angular frequency ($\omega = 2\pi f$max) at which the imaginary part of the impedance ($-Z_{im}$) is maximum and f_{max} is AC frequency at maximum value of $-Z_{im}$, n is the phase shift. From the data of Table 4, it is seen that the polarization resistance values (R_p) are higher in presence of PPs as compared in their absence, which indicates that PPs molecules forms protective film on the metal surface. The double layer capacitance (Cdl) values can be calculated by using the following equation [47]

$$C_{dl} = \frac{Y\omega^{n-1}}{\sin(n(\pi/2))} \tag{21}$$

where ω is angular frequency ($\omega = 2\pi f_{max}$) at which the imaginary part of the impedance ($-Z_{im}$) is maximum and n is the phase shift. According to Table 4, the C_{dl} values decreases with the addition of inhibitors, due to increase in the electrical double layer at the metal/solution interface and decrease in the local dielectric constant. Also the values of "n" in presence of inhibitors increased revealing that the metal surface becomes smooth due to replacement of water molecules from the metal surface.

The Bode impedance magnitude and phase angle plots recorded for mild steel in 1 M HCl in the absence and presence of the optimum concentration of inhibitors are shown in Fig. 3f. The fitted Bode plots of

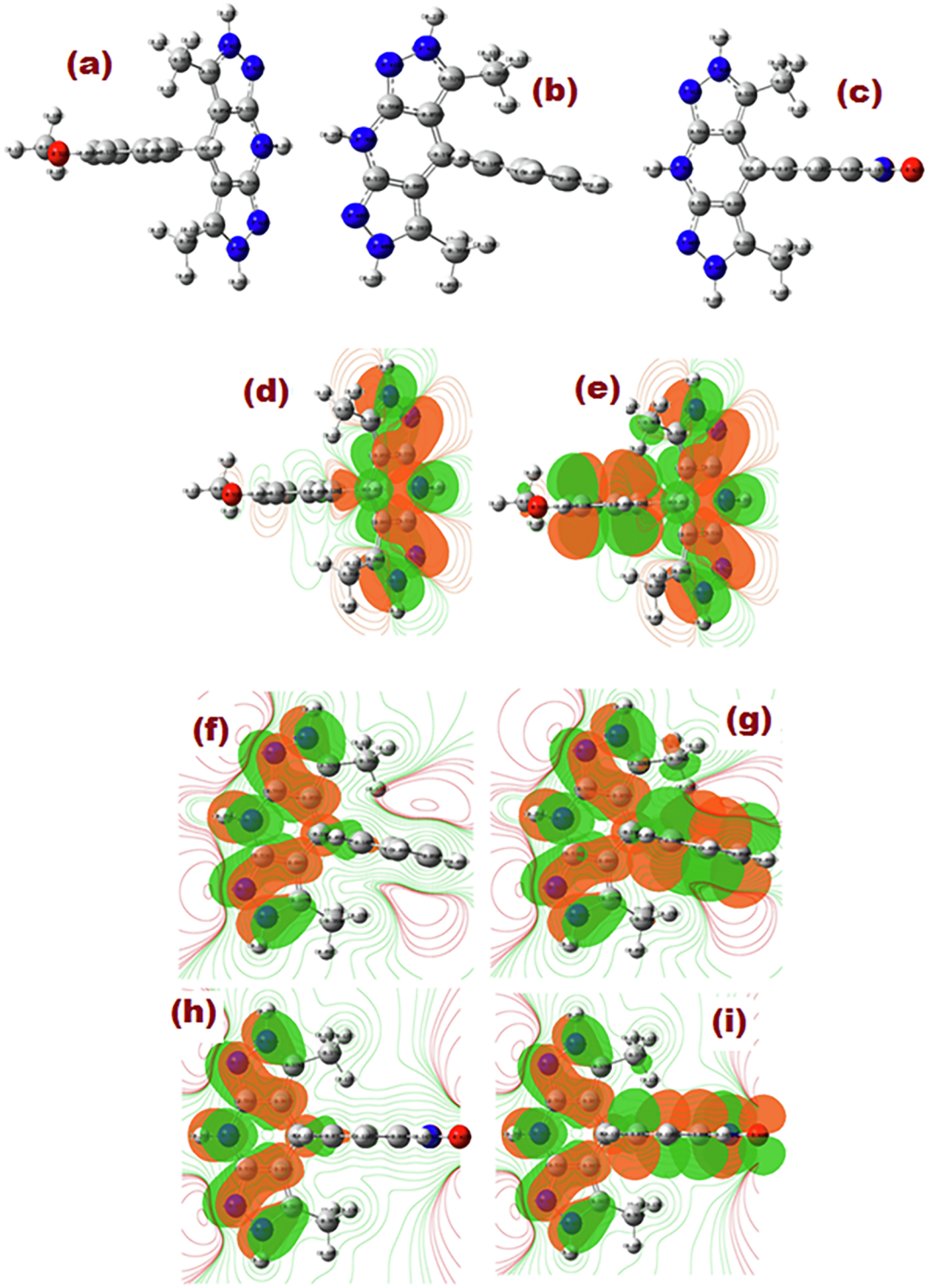

Fig. 7. Optimized and Frontier molecular orbital's of neutral PP-1 (a) HOMO (b) LUMO, PP-2 (c) HOMO (d) LUMO and PP-3 (e) HOMO (f) LUMO of neutral (a) PP-1 (b) PP-2 (c) PP-3.

PPs are shown in Fig. 3 (g-i).

Generally for the ideal capacitor slope and the phase angle values should be −1, and 90° respectively [48]. It is seen that Bode plots involve only one phase maximum revealing that corrosion process takes place in one step, which corresponds to one time constant [44]. It is also seen that from Fig. 3f that phase angle values is less than −90°, which signified the non ideal behavior of capacitor. For the present case the phase angle values is less than −90°, which signified the non ideal behavior of the capacitor. The more negative value of phase angle and the high value of absolute impedance in the presence of PPs indicate the superior performance of PPs [49].

Potentiodynamic polarization

The potentiodynamic polarization plot in the absence and presence of PPs in 1 M HCl at 308 K are shown in Fig. 4. Potentiodynamic polarization parameters were evaluated such as corrosion potential (E_{corr}),

Table 7
Different DFT parameters derived for neutral and protonated form of PP molecules.

Inhibitors	μ (Debye)	E_{HOMO}	E_{LUMO}	ΔE	η	$^{b}\sigma$	χ	ΔN
	Neutral form All energy values are in eV; $^{b}\sigma$ is in eV^{-1}							
PP-1	2.855	−5.320	−1.048	4.272	2.136	0.4681	3.184	0.3829
PP-2	3.003	−5.421	−1.033	4.388	2.194	0.4557	3.227	0.3630
PP-3	3.384	−5.812	−1.029	4.783	2.391	0.4148	3.4205	0.2925
	Protonated form All energy values are in eV; $^{b}\sigma$ is in eV^{-1}							
PP-1	11.155	−7.541	−5.463	2.078	1.039	0.9624	6.502	−0.8094
PP-2	8.025	−9.736	−5.321	4.415	2.207	0.4530	7.528	−0.6134
PP-3	7.2935	−9.681	−5.141	4.540	2.270	0.4405	7.411	−0.5767

Table 8
Fukui functions on different atoms of the neutral as well as protonated forms of PP molecules.

PP-1	*fk*−	*fk*+	PP-2	*fk*−	*fk*+	PP-3	*fk*−	*fk*+
C1	0.0464	0.0004	C1	0.0000	−0.0050	C1	0.0488	0.0001
C2	0.0435	0.0014	C2	0.0091	0.1732	C2	0.0412	0.0009
C3	−0.0038	0.0025	C3	0.0001	0.3246	C3	−0.0036	0.0007
C4	0.0424	0.0010	C4	0.0001	0.0019	C4	0.0405	0.0006
C5	0.0428	0.0004	C5	0.0000	0.1786	C5	0.0449	0.0001
N6	0.2049	0.0000	N6	0.0002	0.3062	N6	0.2020	0.0000
N7	0.1753	0.0000	N7	0.0488	0.0007	N7	0.1749	0.0001
N8	0.0470	0.0002	N8	0.0412	0.0110	N8	0.0445	0.0001
C9	0.0742	0.0007	C9	−0.0036	−0.0002	C9	0.0788	0.0002
N10	0.1675	0.0001	C10	0.0404	0.0063	N10	0.1665	0.0001
N11	0.0475	0.0004	C11	0.0449	0.0011	N11	0.0449	0.0002
C12	0.0783	0.0005	N12	0.2021	0.0001	C12	0.0829	0.0003
C13	−0.0036	0.0008	N13	0.1749	0.0003	C13	0.0091	−0.0052
C14	−0.0035	0.0004	N14	0.0444	0.0005	C14	0.0000	0.1340
C15	0.0092	−0.0146	C15	0.0787	0.0007	C15	0.0003	0.0559
C16	0.0000	0.2046	N16	0.1666	0.0000	C16	0.0001	0.1453
C17	0.0002	0.2848	N17	0.0449	0.0004	C17	0.0001	−0.0036
C18	0.0000	−0.0118	C18	0.0829	0.0014	C18	0.0001	0.2027
C19	0.0001	0.2254	C19	−0.0038	0.0006	N19	0.0000	0.1837
C20	0.0001	0.3041	C20	−0.0037	0.0005	O20	0.0001	0.1447
O21	0.0000	0.0003					O21	0.1454
C22	0.0000	0.0023					C22	0.0007
							C23	0.0003

anodic Tafel slopes (β_a), cathodic Tafel slopes (β_c), corrosion current density (i_{corr}) are listed in Table 5. From the Fig. 4, it could be observed that both the anodic and cathodic Tafel curves are shifting towards lower current density, indicating that the PPs reduced both the anodic and cathodic corrosion reactions. Table 5 further reveals that very slight change occurs in the values of β_a in the presence of inhibitors but a more pronounced change occurs in β_c values. This indicates that in presence of inhibitors both the anodic and cathodic reactions are affected but the affect is more pronounced on the cathodic reactions. Thus, the inhibitors are mixed type, but predominantly cathodic [50,51]. Also the shift in E_{corr} is towards more negative sides i.e. cathodic with respect to blank suggesting their predominant cathodic behavior. It is clear from Table 5 that the values of corrosion current density (i_{corr}) significantly decreased in presence of inhibitors than in their absence, suggesting their effectiveness as corrosion inhibitors (Table 6).

Surface study

Scanning electron microscopy (SEM) study was used for determining the surface morphology of mild steel. On the inspection of SEM micrograph, the surface of uninhibited specimen is rough and damaged due to the dissolution of metal [Fig. 5(a)]. However in the presence of optimum concentration (100 mg L^{-1}) of PP-1, PP-2 and PP-3 the specimens surface becomes relatively smooth (Fig. 5b-d), which indicate the presence of protective film of PPs [52] on the metal surface. The three dimensional (3D) AFM morphologies for uninhibited and inhibited samples are shown in Fig. 7 (a-d). The average roughness in absence of inhibitor (Fig. 6 a) is 400 nm. The AFM images in the presence of inhibitors are shown in Fig. 6(b-d) and their average roughness are reduced to 20 nm, 60 nm and 100 nm for PP-1, PP-2, and PP-3 respectively. The maximum reduction in surface roughness was observed for PP-1.

Quantum chemical calculations

Quantum chemical calculations of neutral inhibitor molecules

Quantum chemical calculations using DFT method is one of the most important theoretical tools for understanding the interaction between the inhibitor molecules and metal surface [53–55]. The corrosion inhibition performance of inhibitor can be predicted well with the calculated parameters such as highest occupied molecular orbital (EHOMO), lowest unoccupied molecular orbital (ELUMO), energy gap (ΔE) = (ELUMO-EHOMO, global hardness (η), softness (σ) electronegativity (χ), dipole moments (μ) and the fraction of electron transfer. These parameters are calculated by the optimization of the inhibitor molecules [56–58]. For the present study all the quantum chemical parameters were calculated for neutral and protonated molecules in the gas phase and are shown in Table 7. The optimized structures, HOMO and LUMO electron distribution of neutral PPs are shown in Fig. 7 (a-i).The value of HOMO is mainly related with the electron donating tendency of a molecule. The higher the value of EHOMO, greater is the tendency of the molecules to donate electrons to vacant metal orbitals. The, lower value of ELUMO, refers to tendency of inhibitor molecules to accept electrons from metal surface [59,60]. The value of EHOMO for the studied inhibitors follows the order; PP-3 > PP-2 > PP-1. The

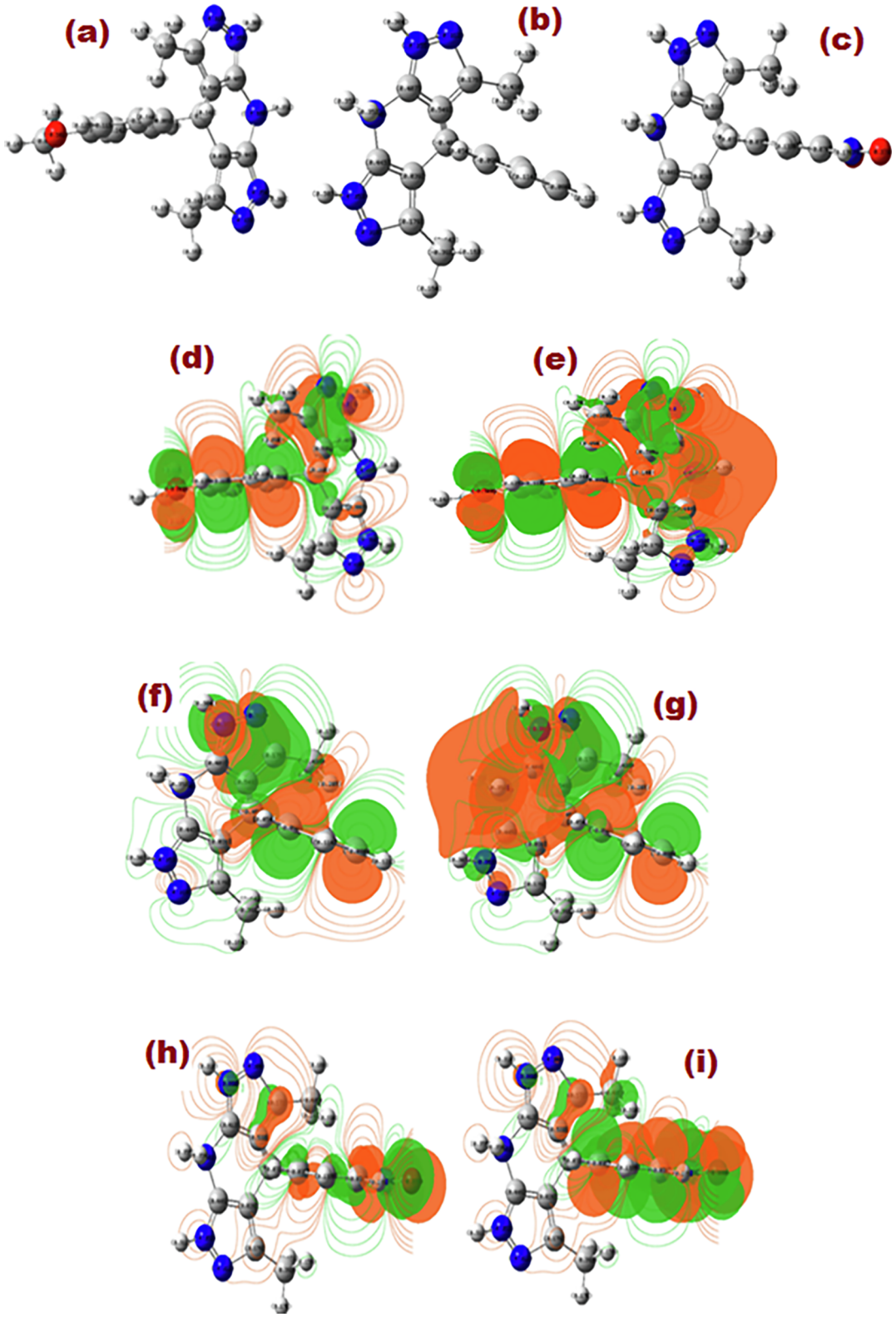

Fig. 8. Optimized structure and Frontier molecular orbital's of protonated PP-1 (a) HOMO (b) LUMO, PP-2 (c) HOMO (d) LUMO and PP-3 (e) HOMO (f) LUMO of protonated (a) PP-1 (b) PP-2 (c) PP-3.

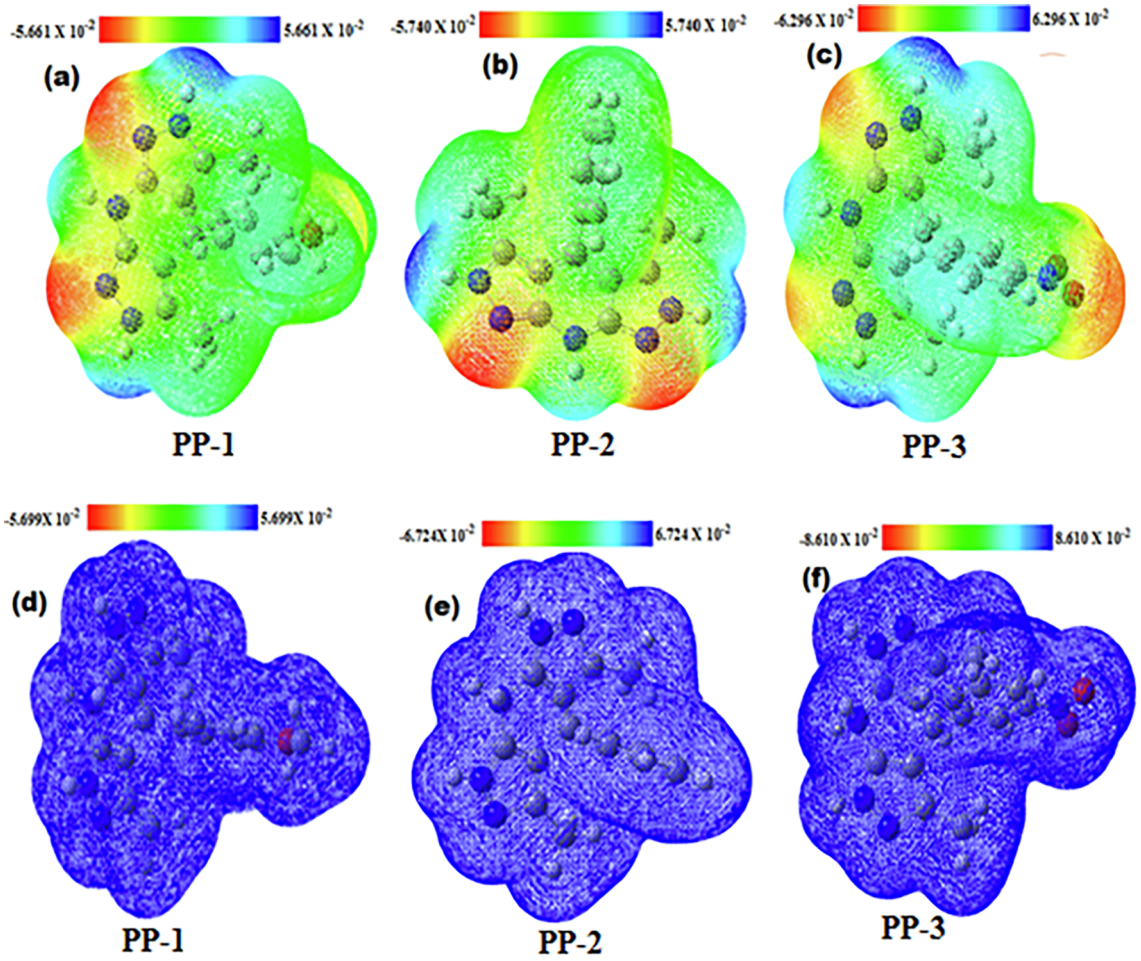

Fig. 9. Electrostatic potential map for neutral and protonated (a-f) PP-1 (b) PP-2 (c) PP-3 respectively.

experimentally obtained values of inhibition efficiency follow the same trend. From the Fig 7(d-i), it is clear that the HOMO regions of PP-1, PP-2, PP-3, delocalized over the pyrazolo-pyridine ring and LUMO regions of PP-1 and PP-2, reside over the pyrazolo-pyridine as well as substituted methoxy-phenyl ring except methoxy group, and in the case of PP-3, it resides both over the pyrazolo-pyridine ring and the substitutedNO2 phenyl ring. Generally a molecule having low value of ΔE correlated with the high chemical reactivity and high inhibition efficiency. From Table 7, it is clear that, PP-1 is the best inhibitor due to its lowest ΔE value as compared to PP-2 and PP-3.

The others quantum chemical parameters have also been calculated and are given in Table 7. A chemical species with high value of softness (σ) and lower value of hardness (η) is associated with the strong interaction with metal and the high IE. In the present case the order of softness (σ) is as follows: PP-1 > PP-2 > PP-3, and the hardness follows the order: PP-3 > PP-2 > PP-1. The obtained results reveal that PP-1 has more electrons donating capacity than PP-2 and PP-. The global electronegativity indicates the extent to which a molecule can retain its electrons. The higher value of (χ) can be associated with a lower tendency of electron donation by an inhibitor molecule and vice versa. From the Table 7 it follows the order; PP-3 > PP-2 > PP-1. The fraction of electron transferred (ΔN) form inhibitors to the metal were calculated and listed in Table 7. If $\Delta N < 3.6$, the inhibition efficiency increases with increasing electron-donation ability to the metal surface In the present case all calculated ΔN values are less than 3.6. Also fraction of electron transfer in case of PP-1 is maximum and lowest in case of PP-3.

Fukui index analysis

Fukuii index play key role to understand donor–acceptor interactions between inhibitor and metal surface. These indicesdefine the nucleophilic as well as the electrophilic nature of the inhibitors molecules [15].Higher value of the f_k^- predicts the electrons donation ability of the inhibitors and higher the value of f_k^+ defines the electron acceptance ability of the inhibitors. Table 8 shows the calculated fukuii indices , the most electrophilic regions for PP-1 are on the C(15), C(16), C(17), C(19) and on C(20), while the nucleophilic regions f_k^- are at the C(1), C(2), C(4), C(5), N(6), N(7), N(8), C(9), N(10), N(11), and C(12) respectively. In the case of PP-2 the most favourable sites for electron acceptance (f_k^+) are C(1), C(2), C(5), and N(6) and the nucleophilic regions are spread over the C1, C2, N7, N8, C10, C(11), N(12), N(13), N (14), C(15), N(16), N(17) and over the C(18) respectively. Likewise in the case of PP-3 the f_k^- regions lies on the C(1), C(2), C(4), C(5), N(6), N (7), N(8), C(9), N(10), N(11), and C(12), and the electrophilic regions (electron accepting) f_k^+ reside over C(14), C(15), C(16), C(18), N(19), O(20) and O(21) these atoms respectively.

The analysis of fukuii indexes reveals that pyrazolo-pyridine ring and phenyl ring are the reactive sites and responsible for donor–-acceptor interactions and thus facilitate bonding between metal and inhibitor molecules.

Quantum chemical calculations of protonated inhibitor molecules

Heteroatom having more negative values of Mullikan charge is likely to undergo protonation easily. The optimized structures, HOMO and LUMO distribution are shown in Fig. 8(a-i). An observation of Table 7 reveals that after protonation, the E_{HOMO} values of both inhibitors are shifted towards more negative side compared to that of

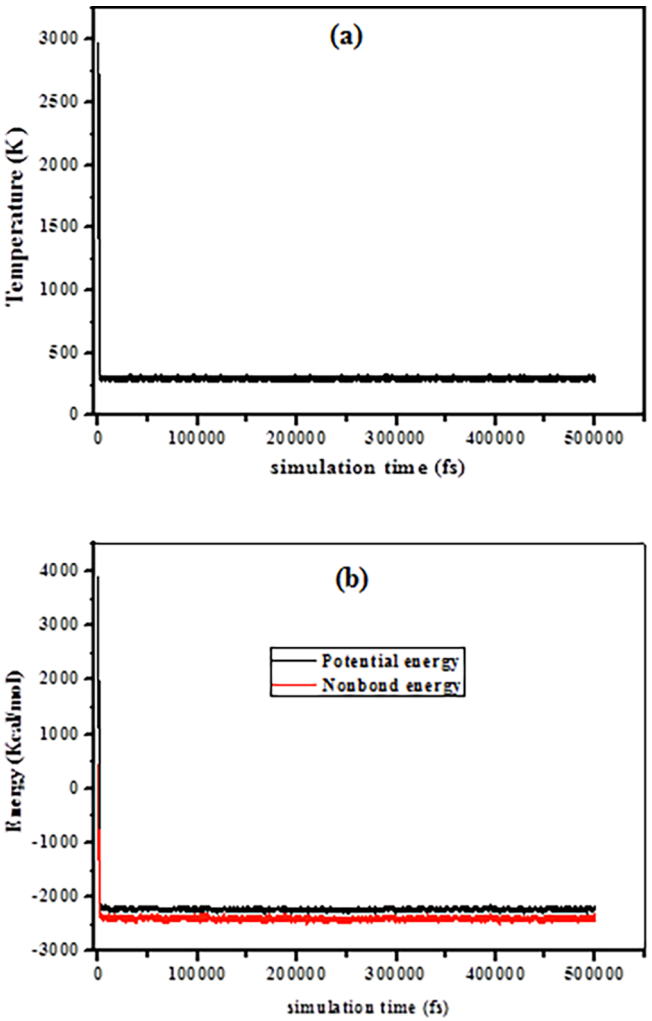

Fig. 10. Temperature (a) and Energy (b) equilibrium curves of studied inhibitors adsorbed on the Fe (1 1 0) surface in solution.

E_{HOMO} values of neutral inhibitors. It suggests that after protonation, the electron donating capability of inhibitors decreased. Furthermore, Table 7 reveals that all the calculated ΔN values in case of inhibitors are negative, which means that the donation of electrons from inhibitor molecules to metal surface is not possible. It is also noted that E_{LUMO} values of protonated inhibitors shift towards more negative side as compared to the neutral, which further suggests that the protonated inhibitors have higher electron accepting capability compared to the neutral form. All these factors cause the change in HOMO and LUMO distribution as compared to the neutral form.

Molecular electrostatic potential

The molecular electrostatic potential (MEP) map gives the information about the low and high electron density sites which is responsible for the electrophilic and nucleophilic attack in the inhibitors molecules. The MEP map of the inhibitors molecule was calculate by the B3LYP/6-31G (d, p) chk file for the neutral and the protonated inhibitors molecules and are shown in the Fig. 9(a-f) respectively. The red color shows the region of the most negative sites and the green color for the zero electrostatic potential. The blue region gives the most positive site of the inhibitor molecules. Fig. 9 (a-c) shows MEP map for neutral molecules for all the three PP-1, PP-2 and PP-3 respectively, the colour region lies in between red - green and blue. The red region occupied by the N atom of the pyrazole-pyridine ring which is the most electronegative sites in the case of PP-1 and PP-2. But in the case of PP-3 the red color region is found over the N atoms of the pyrazole-pyridine rings as well as the NO_2 group of the substituent benzene ring. In the case of 9(d-f) for protonated PP-1, PP-2 and PP-3 the deep blue color region is spread all over the ring which indicates the deficiency of electrons, also tells about that there is no tendency of donating the electrons by all the three inhibitors. These data very well correlates with the data of the ΔN calculated from DFT method.

MD simulations

MD simulations have been used for the study of the interaction between inhibitors and the metal surface [33]. The studies were performed in a system containing 500 water molecules, $5H_3O^+$, 5 $Cl^-$and one molecule of tested inhibitors. Each simulation was run until the system reaches equilibrium. Fig. 10(a) and 10(b) shows that after 500 ps, both the temperature and energy reach balance [61]. Figs. 11 and 12 represent the equilibrium configurations for the three corrosion inhibitors both in the neutral and protonated forms. From the Fig (11 and 12) it is clear that all three inhibitor molecules of both forms were moved gradually near the Fe (1 1 0) surface. And the calculated interaction and the binding energies are given in the Table 9. Higher the negative interaction energy favors higher adsorption ability on the Fe surface of inhibitors molecule and the higher will be the inhibition efficiency whereas the high magnitude of binding energy leads to a more stable inhibitor/surface interaction [62–64]. Based on these data, it can be inferred that the corrosion inhibition performance of studied inhibitors follows the order: PP-1 > PP-2 > PP-3. The presence of electron releasing group (–OCH_3) increasing the adsorption ability of PP-1 [65]. The low interaction energy in case of PP-3 is attributed to the presence of electron withdrawing NO_2 group [34]. The interaction energy protonatedinhibitors with metal are more negative than neutral inhibitors/metal, thereby suggesting that protonated inhibitors are better adsorb than neutral inhibitors. These findings agree well with the experimental results as well as with previously reported studies [45,66].

Diffusion mechanism

MD simulation is considered as reliable method to estimate the diffusion coefficients of corrosive species [67]. In this case, the mean square displacements (MSD) functions were used to investigate the transport of corrosive particles (Cl^- and H_3O^+) inside inhibitor films. A small diffusion coefficient of the corrosive species means strong hinder of simulation system which will induce to high inhibition efficiency [68–71]. The diffusion coefficient is defined as follow [72]:

$$MSD(t) = \left[\frac{1}{N}\sum_{i=1}^{N} |R_i(t) - R_i(0)|^2\right] \quad (22)$$

$$D = \frac{1}{6}\lim_{t\to\infty}\frac{d}{dx}\sum_{i}^{n}\left[|R_i(t) - R_i(0)|^2\right] \quad (23)$$

where $|R_i(t) - R_i(0)|^2$ and N are the mean-square displacement (MSD) and number of target molecules respectively, while $R_i(t)$ and $R_i(0)$ are the positions of corrosive species at time t and 0, respectively. Diffusion coefficients have been calculated using the following equation [75]:

$$D = \frac{m}{6}$$

"m" is the slope of MSD curve.

Fig. 13 shows the diffusion models and MSD curves of Cl^- and H_3O^+ in the three corrosion inhibitor films at 303 K. Thus, Table 10 listed the calculated diffusion coefficients of Cl^- and H_3O^+ in three inhibitor films. It can be seen from the Table 1 that the diffusion coefficients of Cl^- and H_3O^+ in the inhibitor film of PP-1, PP-2 and PP-3 follow the order of: $D_{H_3O^+}$(PP-3) > $D_{H_3O^+}$(PP-2) > $D_{H_3O^+}$(PP-1) and D_{Cl^-}(PP-3) > D_{Cl^-}(PP-2) > D_{Cl^-}(PP-1). These results are in accordance with the reported inhibition efficiency [68]. The much smaller diffusion

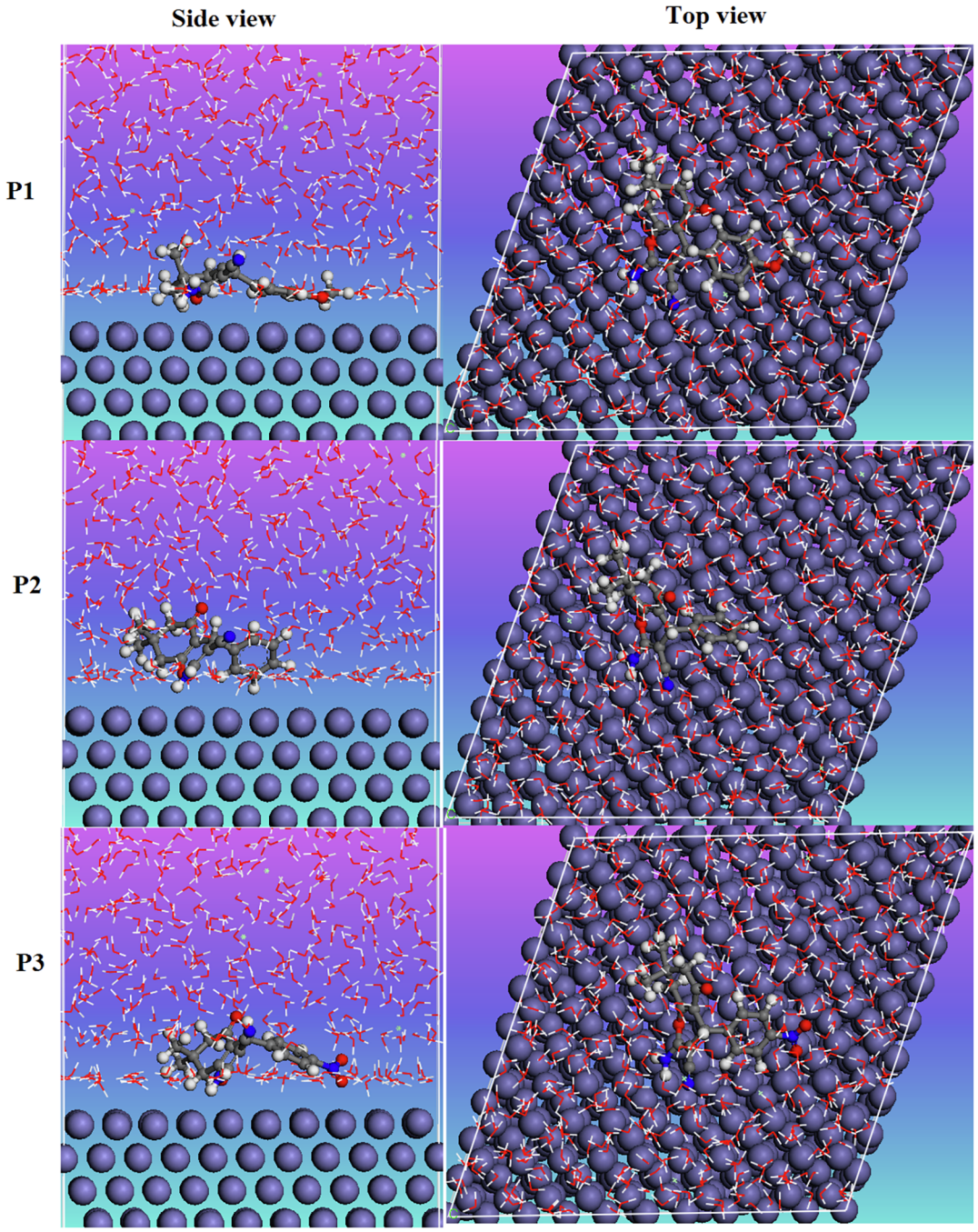

Fig. 11. Side views of the most stable configurations for adsorption of (a) PP-1 (b) PP-2 and PP-3 on Fe (1 1 0) surface calculated using Molecular Dynamics simulations in the neutral phase in the aqueous medium.

coefficients of Cl^- and H_3O^+ in PP-1 indicates that the migration rate of these corrosive species are both be inhibited. This is because; the inhibitor film constrains the diffusion of these particles [66]. It is also apparent from the Table 10 that the diffusion coefficients of Cl^- and H_3O^+ in PP-2 and PP-3 inhibitor film increased comparing with that in PP-1 which indicates the decrease in the inhibitive capacity of these inhibitors against the diffusion of the corrosive particles [72].

Mechanism of inhibition

The following mechanism can be proposed on the basis of experimental and theoretical methods (Fig. 14):

(1) In hydrochloric acid solution pyrazolo-pyridine molecules can exist in protonated and neutral form. The protonated inhibitor can adsorbed on mild steel surface at previously adsorbed chloride ions

$$PP + H^+ \rightleftarrows PP - H^+$$

In the beginning Cl^- ions get adsorbed over the mild steel (MS), which create negative charge on the metal surface. The protonated inhibitor molecules are adsorbed on chloride ions through electrostatic interaction (physical adsorption).

(2) The protonated inhibitor molecules get reduced by accepting the electron from the cathode and become neutral. These neutral

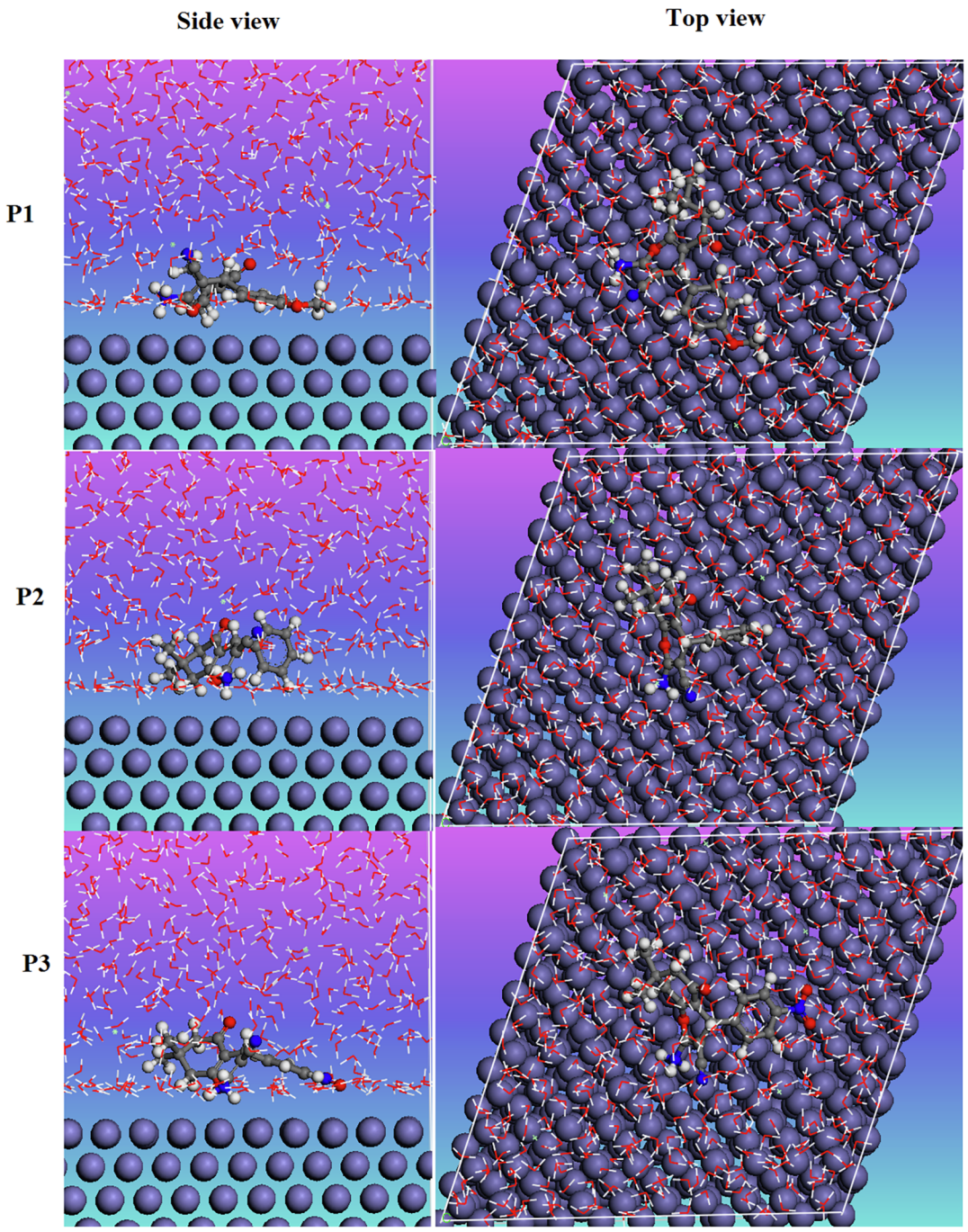

Fig. 12. Side views of the most stable configurations for adsorption of (a) PP-1 (b) PP-2 and PP-3 on Fe (1 1 0) surface calculated using Molecular Dynamics simulations in the protonated phase in aqueous medium.

Table 9
Interaction energies between the inhibitors and Fe (1 1 0) surface (kJ/mol) derived in gas phase.

System	Neutral form		Protonated form	
	$E_{Interaction}$(kJ/mol)	$E_{Binding}$(kJ/mol)	$E_{Interaction}$(kJ/mol)	$E_{Binding}$(kJ/mol)
Fe + **P-1** + 500H_2O + 5H_3O^+ + 5Cl^-	−701.13	701.13	−743.70	743.70
Fe + **P-2** + 500H_2O + 5H_3O^+ + 5Cl^-	−673.11	673.11	−711.51	711.51
Fe + **P-3** + 500H_2O + 5H_3O^+ + 5Cl^-	−562.51	562.51	−652.33	652.33

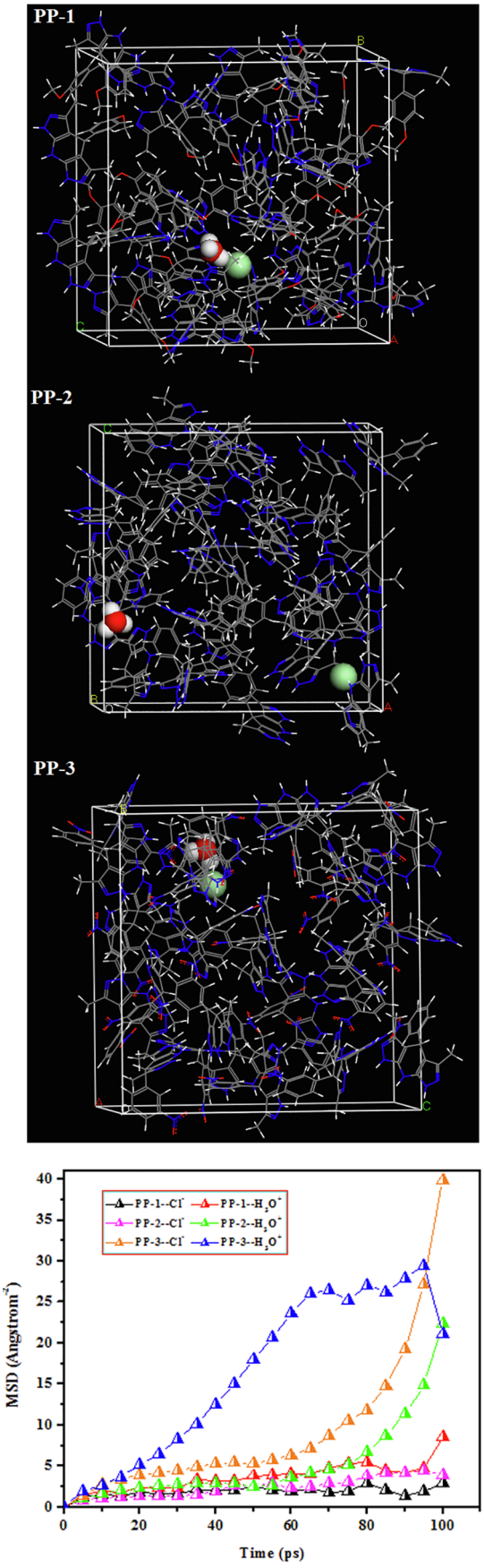

Fig. 13. The diffusion models and MSD curves of Cl^- and H_3O^+ in the three corrosion inhibitor films at 303 K.

Table 10
The diffusion coefficient values of Cl^- and H_3O^+ at 303 K.

System	$D_{H_3O^+}$ (10^{-9} m^2/s)	D_{Cl^-} (10^{-9} m^2/s)
PP-1	0.0086	0.0021
PP-2	0.0410	0.0065
PP-3	0.0515	0.0227

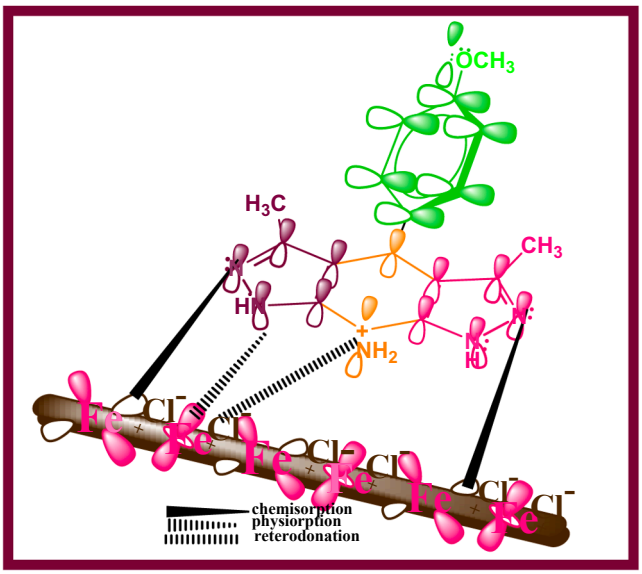

Fig. 14. Schematic adsorption and inhibition mechanism of PP-1 molecule.

inhibitor molecules are chemically adsorbed on metal surface through their lone pair of electrons [12].

(3) Further back-bonding (reterodonation) occurs between the inhibitor and the metal surface, which strengthen the adsorption of inhibitor molecules.

Conclusions

1. All the three pyrazolo-pyridines (PPs) acted as excellent corrosion inhibitors.
2. Among the three PPs, PP-1 having methoxy substituent exhibited highest inhibition efficiency of 97.58% at 100 mg L^{-1}.
3. All the pyrazolo-pyridine were found to inhibit corrosion by adsorption mechanism which followed by Langmuir adsorption isotherm.
4. The formation of protective film was confirmed by SEM and AFM methods.
5. PDP study revealed that all the three PPs act as mixed type corrosion inhibitors, the high value of polarization resistance (Rp) obtained from EIS data further confirmed the effectiveness of studied corrosion inhibitors.
6. The I.E. predicted from theoretical data such as, E_{HOMO}, E_{LUMO}, ΔE obtained by DFT approach was very well correlated with experimentally obtained I.E.
7. The binding energy calculated by MD method was also in good agreement with the experimental results, and accordingly the binding energy of PP-1 was the highest.
8. The I.E. ranking for the studied inhibitors can be presented as follows; PP-1 > PP-2 > PP-3. The highest I.E of PP-1 was attributed to its parallel adsorption on the metal surface.

Acknowledgement

The author Parul Dohare gratefully acknowledges the financial support of ministry of Human Resources and Development (M.H.R.D.), New Delhi provided as Senior Research Fellowship.

Appendix A. Supplementary data

Supplementary data to this article can be found online at https://doi.org/10.1016/j.rinp.2019.102344.

References

[1] Nasir Baig RB, Varma RS. Alternative energy input: mechanochemical, microwave and ultrasound-assisted organic synthesis. Chem Soc Rev 2012;41:1559.
[2] Dandia A, Singh R, Bhaskaran S. Facile stereoselective synthesis of spiro[indole-oxiranes] by combination of phase transfer catalyst and ultrasound irradiation and their bioassay. Ultrason Sonochem 2011;18:1113.
[3] Joshi RS, Mandhane PG, Diwakar DS, Gill CH. Ultrasound assisted green synthesis of bis(indol-3-yl)methanes catalyzed by 1-hexenesulphonic acid sodium salt. Ultrason Sonochem 2010;17:298.
[4] Dandia A, Bhati DS, Jain AK, Sharma GN. Ultrasound promoted clay catalyzed efficient and one pot synthesis of substituted oxindoles. Ultrason Sonochem 2011;18:1143.
[5] Nabid MR, Rezaei SJT, Ghahremanzadeh R, Bazgir A. Ultrasound-assisted one-pot, three-component synthesis of 1H-pyrazolo[1,2-b]phthalazine-5,10-diones. Ultrason Sonochem 2010;17:159.
[6] Li JT, Yin Y, Sun MX. An efficient one-pot synthesis of 2,3-epoxyl-1,3-diaryl-1-propanone directly from acetophenones and aromatic aldehydes under ultrasound irradiation. Ultrason Sonochem 2010;17:363.
[7] Chavatte P, Yous S, Marot C, Baurin N, Lesieur D. Threedimensional quantitative structure−activity relationships of cyclooxygenase-2 (COX-2) inhibitors: a comparative molecular field analysis. J Med Chem 2001;44:3223.
[8] Stika CS, Gross GA, Leguizamon G, Gerber S, Levy R, Mathur A, et al. prospective randomized safety trial of celecoxib for treatment of preterm labor. Am J Obstet Gynecol 2002;187:653.
[9] Dilger K, Herrlinger C, Peters J, Seyberth HW, Schweer H, Klotz U. Effects of celecoxib and diclofenac on blood pressure, renal function, and vasoactive prostanoids in young and elderly subjects. J Clin Pharmacol 2002;42:985.
[10] Liu C, Li Z, Zhao L, Shen Li. One-step, facile synthesis of pyrazolopyridines and tetrahydropyrazolopyridines through disproportionation of initially formed pyrazolo Hantzschdihydropyridine. ARKIVOC 2009;2:258.
[11] Balamurugan K, Perumal S, Menéndez JC. New four component reactions in water: a convergent approach to the metal free synthesis of spiro[indoline/acenaphthylene-3,4′-pyrazolo[3,4-b]-pyridine derivatives. Tetrahedron 2011;67:3201.
[12] Quiroga J, Portillo S, Pérez A, Gálvez J, Abonia R, Insuasty B. An efficient synthesis of pyrazolo[3,4-b]pyridine-4-spiroindolinones by a three-component reaction of 5-aminopyrazoles, isatin, and cyclic β-diketones. Tetrahedron Lett 2011;52:2664.
[13] Rahmati A. Synthesis of 4-aryl-3-methyl-6-oxo-4,5,6,7-tetrahydro-2H-pyrazolo[3,4-b]-pyridine-5-carbonitrile via a one-pot, three component reaction. Tetrahedron Lett 2010;51:2967.
[14] Sorkhabi HA, Shaabani B, Seifzadeh D. Effect of some pyrimidinic Shciff bases on the corrosion of mild steel in hydrochloric acid solution. Electrochim Acta 2016;50:3446.
[15] Yan Ji, Xu Bin, Gong W, Zhang X, Jin X, Ning W, Meng Y, Yang W, Chen Y. Corrosion inhibition of a new Schiff base derivative with two pyridine rings on Q235 mild steel in 1.0M HCl. J Tai Inst Chem E 2016;66:301.
[16] El Mhammedi MA, Fadel S, Chtaini A, Rakib EM, Khouili M. Investigation of the inhibitive effect of pyrazolo [3, 4-b] pyridine on corrosion of stainless steel in 1.0 M HCl solutions. Sci Study Res 2007;VIII. ISSN 1582-540X.
[17] Singh P, Quraishi MA, Gupta SL, Dandia A. Investigation of the corrosion inhibition effect of3-methyl-6-oxo-4-(thiophen-2-yl)-4,5,6,7-tetrahydro-2H-pyrazolo[3,4-b] pyridine-5-carbonitrile (TPP) on mild steel in hydrochloric acid. J Tai Univ Sci 2016;10:139.
[18] Dohare P, Ansari KR, Quraishi MA, Obot IB. Pyranpyrazole derivatives as novel corrosion inhibitors for mild steel useful for industrial pickling process: experimental and Quantum Chemical study. J Ind Eng Chem 2017;52:197.
[19] Dabiri M, Salehi P, Koohshari M, Hajizadeh Z, MaGeec DI. An efficient synthesis of tetrahydropyrazolopyridine derivatives by a one-pot tandem multi-component reaction in a green media. ARKIVOC 2014;4:204.
[20] ASTM, G 31–72, American Society for Testing and Materials, Philadelphia, PA, 1990.
[21] Dohare P, Chauhan DS, Hammouti B, Quraishi MA. Experimental and DFT investigation on the corrosion inhibition behavior of expired drug lumerax on mild steel in hydrochloric acid. Anal Bioanal Electrochem 2017;9:762.
[22] Adardour K, Touir R, El bakri M, Larhzil H, EbnTouhami M, Ramli Y, Zarrouk A, El Kafsaoui H, Essassi EM. Thermodynamic properties and comparative studies of quinoxaline derivatives as a corrosion inhibitor for mild steel in 1M H_2SO_4. Res Chem Intermed 2015;41:1571.
[23] Becke AD. J Chem Phys 1993;98:1372.
[24] Frisch MJ, Trucks GW, Schlegel HB, Scuseria GE, Robb MA. Gaussian 03. Wallingford, CT: Gaussian Inc.; 2004.
[25] Singh A, Ansari KR, Haque J, Dohare P, Lgaz H, Salghi R, Quraishi MA. Effect of electron donating functional groups on corrosion inhibition of mild steel in hydrochloric acid: experimental and quantum chemical study. J Tai Inst Chem Eng 2017.
[26] Gupta RK, Malviya M, Verma C, Quraishi MA. Aminoazobenzene and diaminoazobenzene functionalized graphene oxides as novel class of corrosion inhibitors for mild steel: experimental and DFT studies. Mat Chem Phys 2017;1:360.
[27] Márquez JS, Zorrilla D, Coronilla AS, de los Santos DM, Navas J, Fernández-Lorenzo C, Calleja JM, Alcántara R. Introducing "UCAFUKUI" software: reactivity-index calculations. J Mol Model 2014;20:1.
[28] Cao Z, Tang Y, Cang H, Xu J, Lu G, Jing W, et al. benzimidazole derivatives as corrosion inhibitors of mild steel in the acidic media. Part II: theoretical studies. Corros Sci 2014;83:292.
[29] Martinez S. Inhibitory mechanism of mimosa tannin using molecular modeling and substitutional adsorption isotherms. Mater Chem Phys 2003;77:97.
[30] Obot IB, Gasem ZM. Theoretical evaluation of corrosion inhibition performance of some pyrazine derivatives. Corros Sci 2014;83:359.
[31] Materials Studio, Revision 6.0, Accelrys Inc., San Diego, USA, 2013.
[32] Verma C, Olasunkanmi LO, Quadri TW, Sherif E-SM, Ebenso EE. Gravimetric, electrochemical, surface morphology, DFT, and Monte Carlo simulation studies on three N-substituted 2-aminopyridine derivatives as corrosion inhibitors of mild steel in acidic medium. J Phys Chem C 2018;122:11870–82.
[33] Saha SK, Dutta A, Ghosh P, Sukul D, Banerjee P. Adsorption and corrosion inhibition effect of Schiff base molecules on the mild steel surface in 1 M HCl medium: a combined experimental and theoretical approach. Phys Chem Chem Phys 2015;17:5679.
[34] Saha SK, Dutta A, Ghosh P, Sukul D, Banerjee P. Novel Schiff-base molecules as efficient corrosion inhibitors for mild steel surface in 1 M HCl medium: experimental and theoretical approach. Phys Chem Chem Phys 2016;18:17898–911.
[35] Chaubey N, Yadav DK, Singh VK, Quraishi MA. A comparative study of leaves extracts for corrosion inhibition effect on aluminium alloy in alkaline medium. Ain Shams Eng J 2017;8:673–82. https://doi.org/10.1016/j.asej.2015.08.020.
[36] Noor EA, Al-Moubaraki AH. Thermodynamic study of metal corrosion and inhibitor adsorption processes in mild steel/1-methyl-4[4′(-X)-styryl pyridinium iodides/hydrochloric acid systems. Mater Chem Phys 2008;110:145.
[37] Abdallah M. Ethoxylated fatty alcohols as corrosion inhibitors for dissolution of zinc in hydrochloric acid. Corros Sci 2003;45:2705.
[38] Larabi L, Harek Y, Benali O, Ghalem S. Hydrazide derivatives as corrosion inhibitors for mild steel in 1 M HCl. Prog Org Coat 2005;54:256.
[39] Amar H, Tounsi A, Makayssi A, Derja A, Benzakour J, Outzourhit A. Corrosion inhibition of Armco iron by 2-mercaptobenzimidazole in sodium chloride 3% media. Corros Sci 2007;49:2936.
[40] Li X, Deng S, Fu H. Three pyrazine derivatives as corrosion inhibitors for steel in 1.0 M H2SO4 solution. Corros Sci 2011;53:3241.
[41] Shuduan D, Xianghong Li, Xiaoguang X. Hydroxymethyl urea and 1,3-bis(hydroxymethyl) urea as corrosion inhibitors for steel in HCl solution. Corros Sci 2014;80:276.
[42] Hu K, Zhuang J, Zheng C, Ma Z, Yan L, Gu H, et al. Effect of novel cytosine-l-alanine derivative based corrosion inhibitor on steel surface in acidic solution. J Mol Liq 2016;222:109.
[43] Oguzie EE, Enenebeaku CK, Akalezi CO, Okoro SC, Ayuk AA, Ejike EN. Adsorption and corrosion-inhibiting effect of Dacryodis edulis extract on low-carbon-steel corrosion in acidic media. J Collo Int Sci 2010;349:283.
[44] Krishnaveni K, Ravichandran J. Influence of aqueous extract of leaves of Morindatinctoria on copper corrosion in HCl medium. J Electroanal Chem 2014;735:24.
[45] Khamis A, Saleh MM, Awad MI, El-Anadouti BE. Enhancing the inhibition action of cationic surfactant with sodium halides for mild steel in 0.5 M H2SO4. Corros Sci 2014;74:83.
[46] Yadav DK, Chauhan DS, Ahamad I, Quraishi MA. Electrochemical behavior of steel/acid interface: adsorption and inhibition effect of oligomeric aniline. RSC Adv 2013;3:632.
[47] Odewunmi NA, Umoren SA, Gasem ZM. Utilization of watermelon rind extract as a green corrosion inhibitor for mild steel in acidic media. J Ind Eng Chem 2015;21:239.
[48] Carranza RM, Alvarez MG. The effect of temperature on the passive film properties and pitting behaviour of a Fe-Cr-Ni alloy. Corros Sci 1996;38:909.
[49] Khaled KF. Studies of iron corrosion inhibition using chemical, electrochemical and computer simulation techniques. Electrochim Acta 2010;55:6523.
[50] Singh P, Quraishi M. Corrosion inhibition of mild steel using Novel Bis Schiff's Bases as corrosion inhibitors: electrochemical and Surface measurement. Measure 2016;86:114.
[51] Chaubey N, Singh VK, Quraishi MA. Effect of some peel extracts on the corrosion behavior of aluminum alloy in alkaline medium. Int J Ind Chem 2015;6:317. https://doi.org/10.1007/s40090-015-0054-8.
[52] Mamosemh M, Duan J, Du X. Investigation of the effect of 4,5-dichloro-2-n-octyl-4-isothiazolin-3-one inhibition on the corrosion of carbon steel in Bacillus sp. inoculated artificial seawater. Corros Sci 2013,;69:338.
[53] Hassan HH, Abdelghani E, Amin MA. Inhibition of mild steel corrosion in hydrochloric acid solution by triazole derivatives: Part I. Polarization and EIS studies. Electrochim Acta 2007;52:6359.
[54] Goulart CM, Souza AE, Huitle CAM, Rodrigues CJF, Maciel MAM, Echevarria A. Experimental and theoretical evaluation of semicarbazones and thiosemicarbazones as organic corrosion inhibitors. Corros Sci 2013;67:281.
[55] Zhao H, Zhang X, Lin Ji HHu, Li Q. Quantitative structure–activity relationship model for amino acids as corrosion inhibitors based on the support vector machine

and molecular design. Corros Sci 2014;83:261.
[56] Mendonc GLF, Costa SN, Freire VN, Casciano PNS, Correia AN, de Lima- Neto P. Understanding the corrosion inhibition of carbon steel and copper in sulphuric acid medium by amino acids using electrochemical techniques allied to molecular modeling methods. Corros Sci 2017;115:41.
[57] Obayes HR, Al-Amiery AA, Alwan GH, Abdullah TA, Kadhum AAH, Mohamad AB. Sulphonamides as corrosion inhibitor: experimental and DFT studies. J Mol Struct 2017;1138:27.
[58] Solmaz R, Altunbas E, Kardas G. Adsorption and corrosion inhibition effect of 2-((5-mercapto-1, 3, 4-thiadiazol-2-ylimino)methyl)phenol Schiff base on mild steel. Mater Chem Phys 2011;125:796.
[59] Musa AY, Mohamad AB, Kadhum AAH, Takriff MS, Ahmoda W. Quantum chemical studies on corrosion inhibition for series of thio compounds on mild steel in hydrochloric acid. J Ind Eng Chem 2012;18:551.
[60] Zhao P, Liang Q, Li Y. Electrochemical, SEM/EDS and quantum chemical study of phthalocyanines as corrosion inhibitors for mild steel in 1 mol/l HCl. Appl Surf Sci 2005;252:1596.
[61] Musa AY, Kadhum AAH, Mohamad AB, Takriff MS. Molecular dynamics and quantum chemical calculation studies on 4, 4-dimethyl-3-thiosemicarbazide as corrosion inhibitor in 2.5 MH_2 SO_4. Mater Chem Phys 2011;129:660.
[62] Shokry H. Molecular dynamics simulation and quantum chemical calculations for the adsorption of some Azo-azomethine derivatives on mild steel. J Mol Struct 2014;1060:80.
[63] Lgaz H, Salghi R, Jodeh S, Hammouti B. Effect of clozapine on inhibition of mild steel corrosion in 1.0 M HCl medium. J Mol Liq 2017;225:271.
[64] Saha SK, Murmu M, Banerjee P. Evaluating electronic structure of quinazolinone and pyrimidinone molecules for its corrosion inhibition effectiveness on target specific mild steel in the acidic medium: a combined DFT and MD simulation study. J Mol Liq 2016;224:669.
[65] Fouda A, El-Ewady Y, Abo-El-Enien O, Agizah F. Cinnamoylmalononitriles as corrosion inhibitors for mild steel in hydrochloric acid solution. Anti-Corros Methods Mater 2008;55:317.
[66] Zhang D, Tang Y, Qi S, Dong D, Cang H, Lu G. The inhibition performance of long-chain alkyl-substituted benzimidazole derivatives for corrosion of mild steel in HCl. Corros Sci 2016;102:517.
[67] Yan Y, Wang X, Zhang Y, Wang P, Cao X, Zhang J. Molecular dynamics simulation of corrosive species diffusion in imidazoline inhibitor films with different alkyl chain length. Corros Sci 2013;73:123.
[68] Hu SQ, Guo AL, Yan YG, Jia XL, Geng YF, Guo WY. Computer simulation of diffusion of corrosive particle in corrosion inhibitor membrane. Comput Theor Chem 2011;964:176.
[69] Zhang J, Yu W, Yu L, Yan Y, Qiao G, Hu S, et al. Molecular dynamics simulation of corrosive particle diffusion in benzimidazole inhibitor films. Corros Sci 2011;53:1331.
[70] Guo A, Duan G, He K, Sun B, Fan C, Hu S. Synergistic effect between 2-oleyl-1-oleylamidoethyl imidazoline ammonium methylsulfate and halide ion by molecular dynamics simulation. Comput Theor Chem 2013;1015:21.
[71] Xie S-W, Liu Z, Han G-C, Li W, Liu J, Chen Z. Molecular dynamics simulation of inhibition mechanism of 3,5-dibromo salicylaldehyde Schiff's base. Comput Theor Chem 2015;1063:50.
[72] Zhang Z, Tian N, Huang X, Shang W, Wu L. Synergistic inhibition of carbon steel corrosion in 0.5 M HCl solution by indigo carmine and some cationic organic compounds: experimental and theoretical studies. RSC Adv 2016;6:22250.